Yao et al. *Zool. Res.* 2025, 46(2): 469−482
https://doi.org/10.24272/j.issn.2095-8137.2024.335
https://cstr.cn/32248.14.zr.2024.335

ZR | Zoological Research

Article Open Access

Integrated single-cell transcriptomic map of pig kidney cells across various periods and anatomical sites

Tian-Xiong Yao[1,#,*], Na Li[1,#], Lu-Sheng Huang[1,*]

[1] *National Key Laboratory for Swine Genetic Improvement and Germplasm Innovation*, *Ministry of Science and Technology of China*, *Jiangxi Agricultural University*, *Nanchang*, *Jiangxi* 330045, *China*

ABSTRACT

The kidney is essential for maintaining fluid, electrolyte, and metabolite homeostasis, and for regulating blood pressure. The pig serves as a valuable biomedical model for human renal physiology, offering insights across different physiological states. In this study, single-cell RNA sequencing was used to profile 138 469 cells from 12 pig kidney samples collected during the embryonic (E), fattening (F), and pregnancy (P) periods, identifying 29 cell types. Proximal tubule (PT) cells exhibited elevated expression of metabolism-related transcription factors (TFs), including *GPD1*, *ACAA1*, and *AGMAT*, with validation across multiple individuals, periods, and species. Fluorescence homologous double-labeling of paraffin sections further confirmed the expression of *ACAA1* and *AGMAT* in PT cells. Comparative analysis of pig and human kidneys revealed a high degree of similarity among corresponding cell types. Analysis of cell-type heterogeneity highlighted the diversity of thick ascending limb (TAL) cells, identifying a TAL subpopulation related to immune function. Additionally, the functional heterogeneity of kidney-resident macrophages (KRM) was explored across different anatomical sites. In the renal medulla, KRM were implicated in phagocytosis and leukocyte activation, whereas in the renal pelvis, they functioned as ligands, recruiting neutrophils with bactericidal activity to the renal pelvis to combat urinary tract infections.

Keywords: Pig; Kidney; Single-cell RNA sequencing; Periods; Anatomical sites

INTRODUCTION

The kidney plays a vital role in maintaining fluid, electrolyte, and metabolite homeostasis while regulating blood pressure (Alpern et al., 2012; Guyton & Hall, 2005). As interest in kidney health grows, investigating renal function across key physiological periods is essential for understanding adaptive mechanisms and potential pathological processes. During the fattening period, the kidney undergoes metabolic and physiological adjustments postnatally as it matures into a fully functional organ. Pregnancy induces substantial anatomical and physiological modifications, including changes in kidney size, glomerular filtration, and tubular function (Beers & Patel, 2020; van de Velde et al., 2013). Pregnancy-related renal disorders, such as acute kidney injury (AKI) and hypertensive complications (such as preeclampsia), pose significant health risks (Cornelis et al., 2011; Jim & Garovic, 2017; Szczepanski et al., 2020). In individuals with pre-existing chronic kidney disease (CKD), pregnancy-associated hemodynamic changes, such as increased blood volume, impose additional strain on renal function, exacerbating the risk of complications (Fischer, 2007). However, direct investigation of kidney function during pregnancy in humans is limited due to ethical and technical constraints in obtaining renal tissue, impeding our understanding of pregnancy-induced renal adaptations.

In addition to murine models, which are widely used in kidney disease research (Miao et al., 2024), pigs serve as an alternative biomedical model due to their anatomical and physiological similarities to humans (Lunney et al., 2021). Recent advances in single-cell RNA sequencing (scRNA-seq) have enabled detailed characterization of cellular composition and functions in human and murine kidneys, highlighting the complexity and diversity of cellular heterogeneity and regulatory dynamics at single-cell resolution (Lake et al., 2023; Miao et al., 2021; Muto et al., 2021; Stewart et al., 2019). Single-cell/single-nucleus transcriptomic studies in pig are also expanding, offering novel insights into renal physiology (Rao et al., 2023; Wang et al., 2022; Xiao et al., 2024b; Yang et al., 2023; Zhang et al., 2022). Existing scRNA-seq studies of pig kidneys have primarily focused on cell atlas construction, specific cell populations, or pathological conditions (Cheung et al., 2024; Liu et al., 2023; Wang et al., 2022; Zimmerman et al., 2019), but a comprehensive analysis across multiple physiological periods and anatomical regions

Received: 07 December 2024; Accepted: 14 January 2025; Online: 15 January 2025

Foundation items: This work was supported by the International Cooperation and Exchange Program of the National Natural Science Foundation of China (32261133531)

[#]Authors contributed equally to this work

*Corresponding authors, E-mail: TianxiongYao@hotmail.com; Lushenghuang@hotmail.com

remains lacking.

This study employed scRNA-seq to profile 138 469 cells from 12 pig kidney samples spanning embryonic (E), fattening (F), and pregnancy (P) periods, identifying 29 distinct cell types. Proximal tubules (PT) exhibited high expression of metabolism-associated transcription factors (TFs), including *GPD1*, *ACAA1*, and *AGMAT*, with validation across multiple individuals, periods, and species. Fluorescence homologous double-label staining of paraffin sections further confirmed *ACAA1* and *AGMAT* expression in PT cells. Comparative analysis of pig and human kidneys showed a greater level of similarity among corresponding cell types. Investigation of cell-type heterogeneity emphasized the diversity of thick ascending limb (TAL) cells, identifying a cluster of TAL cells related to immune function. Furthermore, functional heterogeneity of kidney-resident macrophages (KRM) was examined across different anatomical sites. In the renal medulla, KRM were implicated in phagocytosis and leukocyte activation, whereas in the renal pelvis, they acted as ligands, recruiting neutrophils with bactericidal activation to the renal pelvis to combat urinary tract infections.

MATERIALS AND METHODS

Ethical approval

The Animal Ethics Committee of Jiangxi Agricultural University approved all experiments involving pigs (JXAULL-202150).

Pig kidney tissue collection

Twelve kidney samples were obtained from nine healthy Large White pigs across three physiological periods: three individuals during pregnancy (gestational days 107, 110, and 111), two during the fattening period (postnatal day 150), and four during the embryonic period (embryonic days 107, 110, and 111) (Supplementary Table S1). Within 30 min post-mortem, the renal cortex (RC), renal medulla (RM), and renal pelvis (RP) were excised and immediately immersed in tissue preservation solution for further processing.

ScRNA-seq tissue isolation and cell suspension preparation

For embryonic and fattening-period pigs, mixed RC, RM, and RP samples were combined in a 2:2:1 weight ratio. In contrast, for pregnancy-period pigs, each anatomical site was processed as an independent sample. Two distinct tissue dissociation protocols were applied based on sample type (Supplementary Table S2).

Reverse transcription, amplification, and library construction

Single-cell suspensions (2×10^5 cells/mL) in phosphate-buffered saline (PBS, HyClone, USA) were loaded onto a microwell chip using the Singleron Matrix® Single Cell Processing System (China). Barcoding beads were collected from the microwell chip, followed by reverse transcription of mRNA captured by the beads to synthesize cDNA, which was subsequently subjected to PCR amplification. The resulting cDNA was fragmented and ligated with sequencing adapters. The scRNA-seq libraries were constructed using the GEXSCOPE® Single Cell RNA Library Kit (Singleron), following the manufacturer's protocols (Dura et al., 2019). Individual libraries were diluted to 4 nmol/L, pooled, and sequenced on the Illumina NovaSeq 6000 platform (USA) with 150 bp paired-end reads.

Primary analysis of raw read data

Raw sequencing reads were processed using CeleScope v.1.16.2 (https://github.com/singleron-RD/CeleScope) with the Sscrofa 11.1 reference genome to generate gene expression matrices.

Quality control

Quality control, dimensionality reduction, and clustering were performed using Scanpy v.1.9.2 (Wolf et al., 2018) in Python v.3.10.8. Expression matrices were filtered according to the following criteria: (1) cells with fewer than 300 or more than 5 000 detected genes were excluded; (2) cells with a total Unique Molecular Identifier (UMI) count exceeding 30 000 were excluded; (3) cells with mitochondrial content exceeding 35% were excluded; (4) genes expressed in fewer than three cells were excluded; and (5) potential doublet cells predicted by Scrublet v.0.2.3 (Wolock et al., 2019) with a score>0.10 were excluded.

Data merging, integration, and annotation

Filtered gene expression matrices were merged, and data normalization was performed using the NormalizeData function in the Seurat R package (Hao et al., 2021). The FindVariableFeatures function was applied to select the top 2 000 highly variable genes for downstream integration. Experiment batch effect correction was achieved using the FindIntegrationAnchors and IntegrateData functions. The integrated dataset was then scaled with the ScaleData function, followed by principal component analysis (PCA) using the RunPCA function. Dimensionality reduction was conducted with the RunUMAP function, utilizing the top 30 principal components in the Uniform Manifold Approximation and Projection (UMAP) algorithm. Cell clustering was performed with the FindNeighbors function, using the top 30 principal components, and clusters were identified by setting the resolution to 0.8 in the FindClusters function. Five main cell types were annotated, including epithelial cells (EpC), endothelial cells (EC), fibroblasts (Fib), immune cells (IM), and smooth muscle cells (SMC).

Subtype annotation was performed for EpC, IM and EC, with EpC used as a representative example. EpCs were first extracted from the filtered dataset, and raw count matrices were normalized and log-transformed using the scanpy.pp.normalize_total and scanpy.pp.log1p functions in Python. The top 2 000 highly variable genes were selected with scanpy.pp.highly_variable, followed by PCA using scanpy.tl.pca. To eliminate experiment batch effects, data integration was performed with Harmony (Korsunsky et al., 2019). Dimensionality reduction and clustering were executed with scanpy.tl.umap and scanpy.tl.louvain, respectively. Cell clusters were annotated based on canonical marker genes curated from published datasets, including PanglaoDB, The Human Protein Atlas, and existing literature (Balzer et al., 2022; El-Achkar et al., 2021; Franzén et al., 2019; Lake et al., 2023; Uhlén et al., 2015).

Validation of cell-type annotation

Cell annotation accuracy was validated using the FindTransferAnchors and TransferData functions in Seurat, establishing a correspondence between pig kidney cells (query dataset) and reference datasets of human and mouse kidney cells. Prediction scores were computed for each cell and median-averaged across cell types (Reynolds et al., 2021). Publicly available datasets were obtained from 2023

Human Kidney Nature (https://cellxgene.cziscience.com/collections/bcb61471-2a44-4d00-a0af-ff085512674c), 2019 Human Kidney Science (https://explore.data.humancellatlas.org/projects/abe1a013-af7a-45ed-8c26-f3793c24a1f4), and 2021 Mouse Kidney Nature Communications (https://www.ncbi.nlm.nih.gov/geo/query/acc.cgi?acc=GSE157079).

Identification of cell type-specific TFs

Cell type-specific TFs were identified based on gene specificity scores (*tau*), calculated as follows (Suo et al., 2018):

$$tau = \frac{\sum_{i=1}(1-\hat{x}_i)}{n-1}$$
$$\hat{x}_i = \frac{x_i}{\max(x_i)} \quad (1)$$

where x_i represents the average normalized gene expression of a given cell type i, n is the number of cell types, and *tau* represents the gene specificity score for the cell type with the highest gene expression. Cell type-specific TFs were filtered using *tau*>0.8.

Gene regulatory network inference using pySCENIC

Gene regulatory networks were inferred using pySCENIC v.0.12.1 (Aibar et al., 2017; Van de Sande et al., 2020). Filtered raw read counts and a curated list of human TFs were used as inputs for the GRNBoost2 algorithm to identify co-expression modules. Regulons, defined as TF-centered gene regulatory units, were determined by identifying direct target genes while excluding others based on motif enrichment analysis around transcription start sites, using cisTarget databases. The Human TF list was obtained from (https://github.com/aertslab/pySCENIC/blob/master/resources/hs_hgnc_tfs.txt), and the cisTarget database was downloaded from (https://resources.aertslab.org/cistarget/). Regulon activity was quantified using AUCell, which calculates the area under the recovery curve, while the regulon specificity score (RSS) (Cabili et al., 2011; Yanai et al., 2005) was used to identify cell type-specific regulons.

Fluorescence homologous double-label staining of paraffin sections

Paraffin-embedded tissue sections were subjected to a sequential staining protocol to ensure high specificity and fluorescence signal integrity. The sections were first deparaffinized by sequential immersion in three environmental dewaxing solutions for 10 min each, followed by dehydration in absolute ethanol (three successive 5 min washes). Rehydration was performed by washing the sections in distilled water. For antigen retrieval, sections were treated with a specific antigen retrieval buffer under controlled conditions to prevent excessive evaporation and tissue drying. Following retrieval, the slides were allowed to cool naturally and were washed three times in PBS (pH 7.4) using a decolorizing shaker, each wash lasting 5 min. To minimize endogenous peroxidase activity, tissue regions were circumscribed using a hydrogen peroxide-sealed histochemical pen and incubated in 3% hydrogen peroxide solution at room temperature for 25 min in the dark. The sections were then washed three times in PBS (pH 7.4) for 5 min per wash. Serum blocking was performed by drying the PBS and adding bovine serum albumin (BSA). For primary antibodies derived from rabbits, 10% goat serum was used for blocking, while 3% BSA was applied for other primary antibodies. The blocking step was carried out for 30 min to prevent nonspecific binding. Following blocking, the first primary antibody was applied, and the sections were incubated overnight at 4°C in a humidified chamber. After incubation, the slides were washed in PBS (pH 7.4) and incubated with a horseradish peroxidase (HRP)-conjugated secondary antibody for 50 min at room temperature. Excess antibody was removed by three washes in PBS (pH 7.4), each lasting 5 min. Fluorescent labeling was achieved using tyramide signal amplification (TSA). After slight drying, TSA dye was applied to the tissue, and the slides were incubated at room temperature for 10 min in the dark. The reaction was terminated by washing the slides three times in TBST, with each wash lasting 5 min. To enhance antigen retrieval for the second round of labeling, sections were placed in an antigen retrieval buffer and subjected to microwave heating. The heating cycle included 8 min at medium power, followed by 7 min at medium-low power. The same antigen retrieval solution was used as in the initial retrieval step. Following antigen retrieval, the second primary antibody was applied, and the sections were incubated overnight at 4°C in a humidified chamber. After incubation, the slides were washed three times in PBS (pH 7.4), followed by the application of a fluorescent secondary antibody. The sections were incubated at room temperature for 50 min in the dark, then washed three times in PBS (pH 7.4), with each wash lasting 5 min. Nuclei were counterstained with 4’,6-diamidino-2-phenylindole (DAPI) by applying the dye solution to the sections and incubating them at room temperature for 10 min in the dark. To reduce background autofluorescence, the sections were washed three times in PBS (pH 7.4) and incubated with an autofluorescence quenching solution for 5 min, followed by a 10 min rinse in distilled water. If fluorescence signal preservation was required for specific tissue structures, this quenching step was omitted. The sections were mounted using an anti-fading fluorescence mounting medium to ensure long-term fluorescence signal stability. Imaging was performed with the following excitation and emission wavelengths: DAPI (330–380 nm / 420 nm), 488 nm channel (465–495 nm / 515–555 nm), CY3 (510–560 nm / 590 nm), and CY5 (608–648 nm / 672–712 nm).

Cross-species integration analysis

Publicly available human kidney scRNA-seq data (2023 Human Kidney Nature) were obtained from https://cellxgene.cziscience.com/collections/bcb61471-2a44-4d00-a0af-ff085512674c. Healthy adult human kidney cells were extracted from this dataset and integrated with pig kidney cells from the fattening (F) and pregnancy (P) periods. Normalization was performed using the NormalizeData function, and the top 2 000 variable genes were identified using the FindVariableFeatures function. Data integration was conducted using the FindIntegrationAnchors and IntegrateData functions, followed by scaling with the ScaleData function and dimensionality reduction via PCA using the RunPCA function. Integrated datasets were visualized using UMAP plots, with cell types from human and pig samples distinguished by color. Cell types represented by fewer than 30 cells were excluded, and the remaining cell populations were reclassified based on cross-species annotation.

Cross-species cell type similarity analysis

Cell type similarity across species was quantified using MetaNeighbor (Crow et al., 2018), allowing for the systematic assessment of conserved cellular identity between human and

pig kidney cells.

Disease module identification using the OMIM database

Disease association analysis was performed based on a previously established statistical approach (Eraslan et al., 2022). A total of 229 disease-topic models were constructed using clinical feature similarity data from the Online Mendelian Inheritance in Man (OMIM) database (Amberger et al., 2019).

Heterogeneity of TAL cells

TAL cells were extracted from the filtered dataset, and the raw count matrix was normalized and log-transformed using the scanpy.pp.normalize_total and scanpy.pp.log1p functions in Python. The top 2 000 highly variable genes were selected using scanpy.pp.highly_variable, and PCA was performed using the scanpy.tl.pca function. Experiment batch effect correction was applied using Harmony to ensure data integration. Dimensionality reduction was performed using scanpy.tl.umap, and clustering was performed using scanpy.tl.louvain at a resolution of 0.5.

TAL pseudo-cell construction

To enhance resolution in TAL subtype analyses, pseudo-cell populations were generated by randomly aggregating raw read counts from groups of 50 TAL cells within each subtype.

Weighted gene co-expression network analysis (WGCNA)

Pseudo-cell datasets for each TAL subtype were merged, and gene filtering was conducted using OGFSC in R (Hao et al., 2019). Co-expression network analysis was performed using the WGCNA package in R (Langfelder & Horvath, 2008) to identify gene modules associated with TAL cell function.

Pathway enrichment analysis

Functional enrichment analysis was conducted using the ClueGO plugin (Bindea et al., 2009) in Cytoscape. The Benjamini-Hochberg method was employed for multiple testing correction, with a threshold of adjusted $P<0.05$ to define significantly enriched pathways.

Variations in cell type proportions across anatomical sites in the P period

For the P period, a cell type was retained for analysis if it constituted at least 20% of the total kidney cells across all three physiological periods. If below 20%, it was still included if its average cell count per sample exceeded 75 cells. Enrichment of cell types within specific anatomical sites, including the RC, RM, and RP, was assessed using the Speckle package in R (Phipson et al., 2022). A false discovery rate (FDR) threshold of 0.05 was applied to filter out non-significant cell type enrichments.

Cell-cell communication analysis

Intercellular communication networks within the RC, RM, and RP were inferred using CellChat v.1.6.1 in R (Jin et al., 2021). Cell types with fewer than 30 cells per anatomical site were excluded. Significant ligand-receptor interactions ($P<0.05$) between cell populations were retained for downstream analyses.

Stereo-seq data

RM samples were embedded in Tissue-Teck OCT within 30 min post-resection after removing excess fluid. Samples were flash-frozen in dry ice and subsequently stored at −80°C until further processing. Cryosections (10 μm thick) were prepared using a Leica CM1950 cryostat and immediately mounted onto Stereo-seq chips. Spatial transcriptomic data were generated following the STOmics Gene Expression Set-S1 protocol (https://www.stomics.tech/), an optimized version of the original procedure (Chen et al., 2022). Briefly, 10 μm tissue sections were adhered to Stereo-seq chips and incubated for 3 min at 37°C on a slide warmer. Sections were then fixed in −20°C methanol for 30 min, followed by staining with nucleic acid dye (Thermo Fisher, Q10212, USA) and imaging using a Nikon Eclipse Ti-7 microscope (Japan). Following tissue permeabilization for 18 min, cDNA synthesis and purification were performed directly on the Stereo-seq chips. Indexed cDNA libraries were then constructed according to the manufacturer's protocols and sequenced on an MGI DNBSEQ-Tx sequencer (50 bp for read 1, 100 bp for read 2). Post-sequencing, raw *in situ* spatial transcriptomic data underwent quality control and unsupervised clustering, as described previously (Chen et al., 2022). Expression profile matrices were generated using SAW, an analysis pipeline available on GitHub (https://github.com/BGIResearch/SAW). Briefly, invalid CID sequences (tolerating a single-base mismatch) and low-quality UMI sequences (quality score<10) were filtered. Reads were then aligned to the Sscrofa 11.1 reference genome using STAR, and expression matrices were generated. Cell clustering and annotation were performed using Scanpy v.1.10.2.

RESULTS

Single-cell atlas of the pig kidney

To depict the pig kidney cellular landscape, a comprehensive single-cell transcriptomic map was derived from 12 kidney samples collected from nine individuals (five males and four females) across three physiological periods: E (embryonic days 107, 110, and 111), F period (postnatal day 150), and P (pregnancy days 107, 110, and 111). At the P period, the kidney was further subdivided into three anatomical sites, including the RC, RM, and RP (Figure 1A; Supplementary Table S1). Following stringent quality control, 138 469 high-quality single cells were retained, with a median of 828 detected genes per cell. To correct for experiment batch effects, data integration was performed using the FindIntegrationAnchors and IntegrateData functions in Seurat, ensuring effective cross-sample alignment. UMAP visualization confirmed successful batch correction (Supplementary Figure S1A, B). Graph-based Louvain clustering (Levine et al., 2015) identified five major cell types, including epithelial cells (EpC), endothelial cells (EC), immune cells (IM), fibroblasts (Fib), and smooth muscle cells (SMC), using CellID in R (Cortal et al., 2021). Subtype annotation was conducted for the EpC, EC, and IM populations based on canonical marker genes retrieved from public databases (Franzén et al., 2019; Uhlén et al., 2015) and published literature (Balzer et al., 2022; El-Achkar et al., 2021; Lake et al., 2023) (Figure 1B, C). A total of 29 distinct cell types were identified, including renal tubule cells (PT, DTL, TAL, PC, and IC), endothelial subpopulations (ECGC, ECDVR, and ECPTC), and immune cells (T, NKT, B, Plasma, PDC, KRM, and Neu), in addition to Fib and SMC (Figure 1B). These cell types were detected across all samples, spanning both sexes and all periods (Figure 1D). To validate the accuracy of cell annotation, reference datasets were downloaded (Lake et al., 2023; Miao et al., 2021; Stewart et al., 2019). Comparison with these references demonstrated higher prediction scores for corresponding kidney cell types, as assessed using the

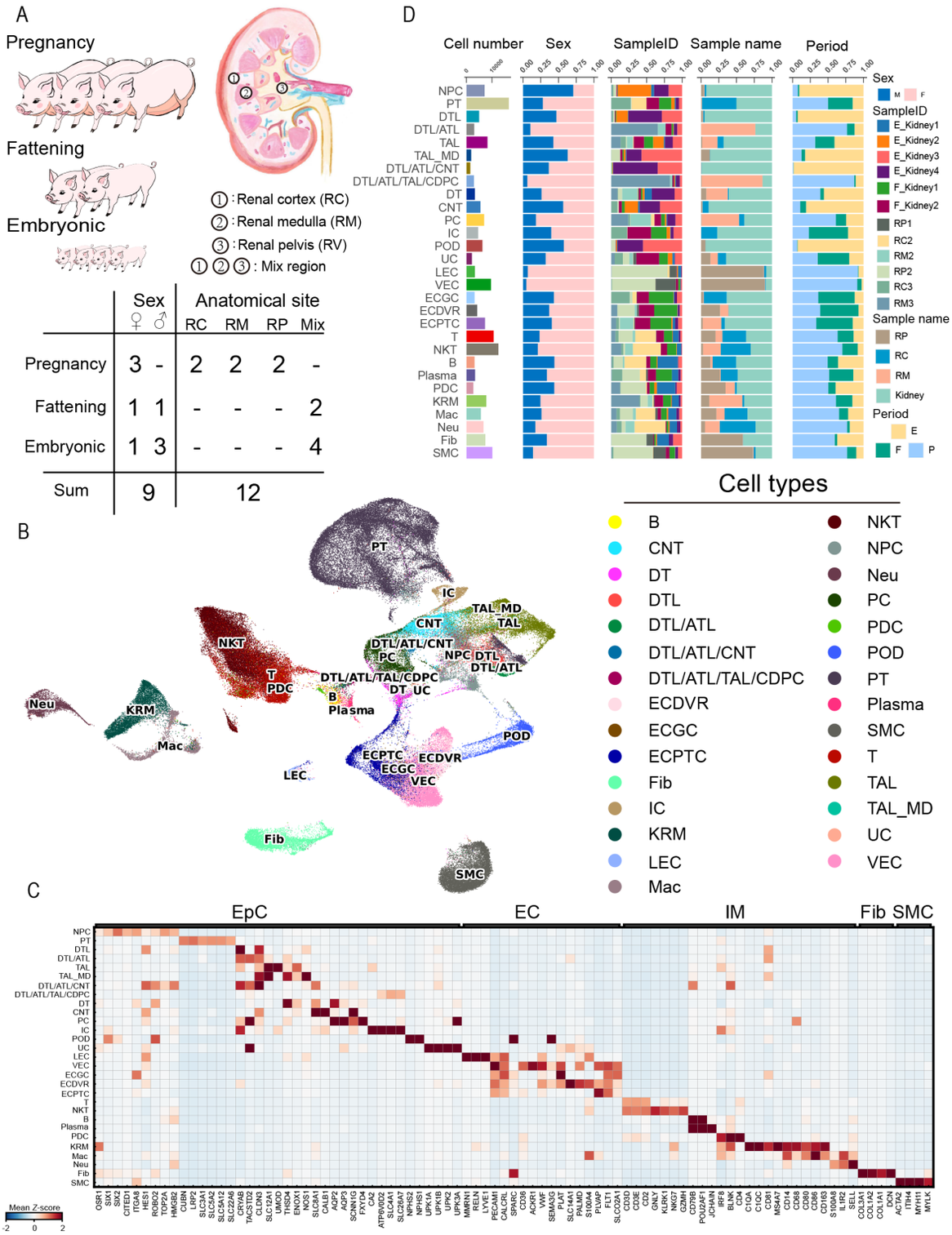

Figure 1 ScRNA-seq identification of kidney cells across multiple periods and anatomical sites

A: Schematic representation of experimental design. B: UMAP visualization of 138 469 cells from 12 samples collected from nine individuals, annotated into 29 distinct cell types, including nephron progenitors (NPC), proximal tubule (PT), descending thin limb (DTL), descending thin limb/ascending thin limb (DTL/ATL), thick ascending limb (TAL), thick ascending limb (macula densa) (TAL_MD), descending thin limb/ascending thin limb/connecting tubule (DTL/ATL/CNT), descending thin limb/ascending thin limb/thick ascending limb/collecting duct principal cells (DTL/ATL/TAL/CDPC), distal tubule (DT), connecting tubule (CNT), principal cells (PC), intercalated cells (IC), podocytes (POD), urothelial cells (UC), lymphatic endothelial cells (LEC), vascular endothelial cells (VEC), glomerular endothelial cells (ECGC), descending vasa recta of endothelial cells (ECDVR), peritubular capillaries of endothelial cells (ECPTC), T cells (T), natural killer T cells (NKT), B cells (B), Plasma, plasmacytoid dendritic cells (PDC), kidney residual macrophages (KRM), macrophages (Mac), neutrophils (Neu), fibroblasts (Fib), and smooth muscle cells (SMC). C: Heatmap of manually selected marker genes for the 29 identified cell types. D: Bar plot summarizing, from left to right, cell count, sex contribution, sample contribution, anatomical site contribution, and period contribution in each cell type.

FindIntegrationAnchors and TransferData functions in Seurat (Supplementary Figure S2A–D).

Cell type-specific TFs and regulatory landscape of the pig kidney

TFs play a crucial role in regulating gene expression, orchestrating cell cycle progression and determining cell fate (Latchman, 1997; Young, 2011). At a *tau* threshold of >0.80, 298 TFs exhibited cell type-specific expression (Figure 2A), including *SIX2* and *UNCX* in NPC, *FOXA1* in UC, *GATA3* in PC, *FOXI1* in IC, *TCF7* in T, and *REL* in Mac. Several well-characterized TFs were enriched in PT cells, including *HNF4A*, a key regulator of PT maturation from PT progenitors. Loss of HNF4A has been shown to lead to developmental arrest of PT progenitors (Marable et al., 2020). Additionally, previously unreported PT-specific TFs were identified. For example, *A1CF* (*tau*=0.93), characterized as an antagonistic factor of kidney fibrosis via epithelial-mesenchymal transition (EMT) inhibition (Huang et al., 2016), was specifically expressed in PT. PT cells also exhibited high expression of metabolism-associated TFs, such as *GPD1* (*tau*=0.84), which contributes to NADH production for ATP synthesis, *AGMAT* (*tau*=0.95), which participates in the urea cycle and amino group metabolism, and *ACAA1* (*tau*=0.85), which plays a role in lipid metabolism (Wanders et al., 2001; Wang et al., 2021b) (Figure 2B). These TF expression patterns were consistently detected across all three physiological periods and multiple individuals in pigs (Supplementary Figure S3A). Fluorescence homologous double-label staining of paraffin-embedded sections further confirmed *ACAA1* and *AGMAT* expression in PT cells (Figure 2C). The expression patterns of these TFs were further examined in other species, including humans (Tabula Sapiens Consortium et al., 2022), *Macaca fascicularis* (Han et al., 2022), *Mus musculus* (Tabula Muris Consortium et al., 2018), using single-cell or single-nucleus RNA-seq data. Results showed that *GPD1* was highly expressed in PT cells across all four species, while *AGMAT* was conserved across three species and *ACAA1* was detected in two species (Supplementary Figure S3B–D).

To further investigate TF-driven regulatory networks and cellular states, Single-cell Regulatory Network Inference and Clustering (SCENIC) (Aibar et al., 2017; Van de Sande et al., 2020) was applied to infer TF regulon activity. SCENIC analysis revealed strong enrichment in UNCX and HOXC10 regulon activity in NPC, HNF4A, HNF4G, MAF, and NR1H4 in PT, ESRRB in TAL (a segment of loop of Henle), GATA3 in PC, FOXI1 in IC, WT1 in POD and FOXA1 in UC (Figure 2D, E; Supplementary Figure S3E). ESRRB is an orphan nuclear receptor essential for early development and pluripotency (Festuccia et al., 2018; Muto et al., 2021), with reported enrichment in TAL cells at the chromatin accessibility level (Muto et al., 2021). *FOXI1*, a TF specifically expressed in IC, is critical for IC differentiation (Blomqvist et al., 2004). *GATA3* has been shown to transactivate *AQP2*, a known PC marker (Uchida et al., 1997). In the present study, *ELF5*, a predicted GATA3 target gene, was highly expressed in PCs (*tau*=0.95) (Supplementary Table S3). Previous studies have demonstrated that *ELF5* activates PC-specific gene promoters and maintains *AQP2* expression levels during kidney development (Grassmeyer et al., 2017).

Human-pig cross-species comparison of kidney cell types

Single-cell transcriptomics enables direct comparisons of cellular composition and transcriptomic dynamics across species. To assess the conservation of kidney cell types, pig kidney scRNA-seq data were integrated with human kidney data (Lake et al., 2023). The integrated dataset comprised 124 952 cells, including 20 490 human cells and 104 462 pig cells (Supplementary Table S4). UMAP visualization demonstrated that most cell types were represented in both species, with corresponding human and pig cell types clustering closely together (Figure 3A, B; Supplementary Figure S4A, B). The similarity of cell types between species was quantified using the mean area under the receiver operating characteristic curve (AUROC) score obtained from MetaNeighbor (Crow et al., 2018). A heatmap comparing human and pig kidney cell types showed that renal tubule epithelial cells (PT and TAL), immune cells (T cells, B cells, pDC, and Mac), endothelial cells (LEC and ECPTC), and SMC were highly conserved across species (AUROC>0.9) (Figure 3C). The findings are consistent with previous cross-species comparative analyses of vertebrate kidney cell types (Geirsdottir et al., 2019; Qu et al., 2022; Wang et al., 2021a). To further investigate cell type differences under pathological conditions, the cell type composition of pig kidneys was compared with those of normal and diseased human kidneys (Abedini et al., 2024). Analysis revealed a lower proportion of PT cells and a higher proportion of T cells in two CKD subtypes —diabetic kidney disease and hypertensive kidney disease—compared to normal human kidneys. In contrast, the cell type composition of normal pig kidneys more closely resembled that of normal human kidneys (Figure 3D). To explore the relationship between cell types and kidney disease, the expression of CKD-associated genes identified by genome-wide association studies (GWAS) was examined. These genes were predominantly expressed in PT cells (Supplementary Figure S4C), consistent with previous findings (Park et al., 2018). A broader investigation into the association between human diseases and specific cell types in the pig kidney identified 36 disease topics associated with distinct kidney cell populations (Supplementary Table S5). Results showed that many disease topics mapped to their expected cell populations (Figure 3E). Inflammatory and immune-related diseases (topics 49, 205, 132, 216, and 199) were associated with B cells, T cells, and macrophages. Vascular and lymphatic diseases (topics 56, 74, and 124) mapped to various endothelial cells, including VEC, LEC, and ECGC. For renal tubule epithelial cells, most disease topics are mapped to the F and P periods, coinciding with functional maturation of the kidney. Topics 143 and 157, which involve impaired uric acid reabsorption, elevated blood ammonia levels, and amino acid transport deficiencies, were associated with PT cells during the F and P periods. Topic 99, linked to abnormal serum aldosterone levels mapped to CNT cells during pregnancy. Topic 116, associated with pseudohypoaldosteronism, a rare salt-wasting disorder of infancy, was mapped to multiple epithelial subtypes, including PT, IC, PC, TAL, and CNT cells during the embryonic period. These findings highlight the high conservation of major kidney cell types between pigs and humans, reinforcing the biomedical relevance of the pig kidney as a model for human renal physiology and disease research.

Functional heterogeneity of TAL cells across multiple periods

TAL cells play a pivotal anatomical and functional role in renal physiology and electrolyte balance regulation (Balzer et al.,

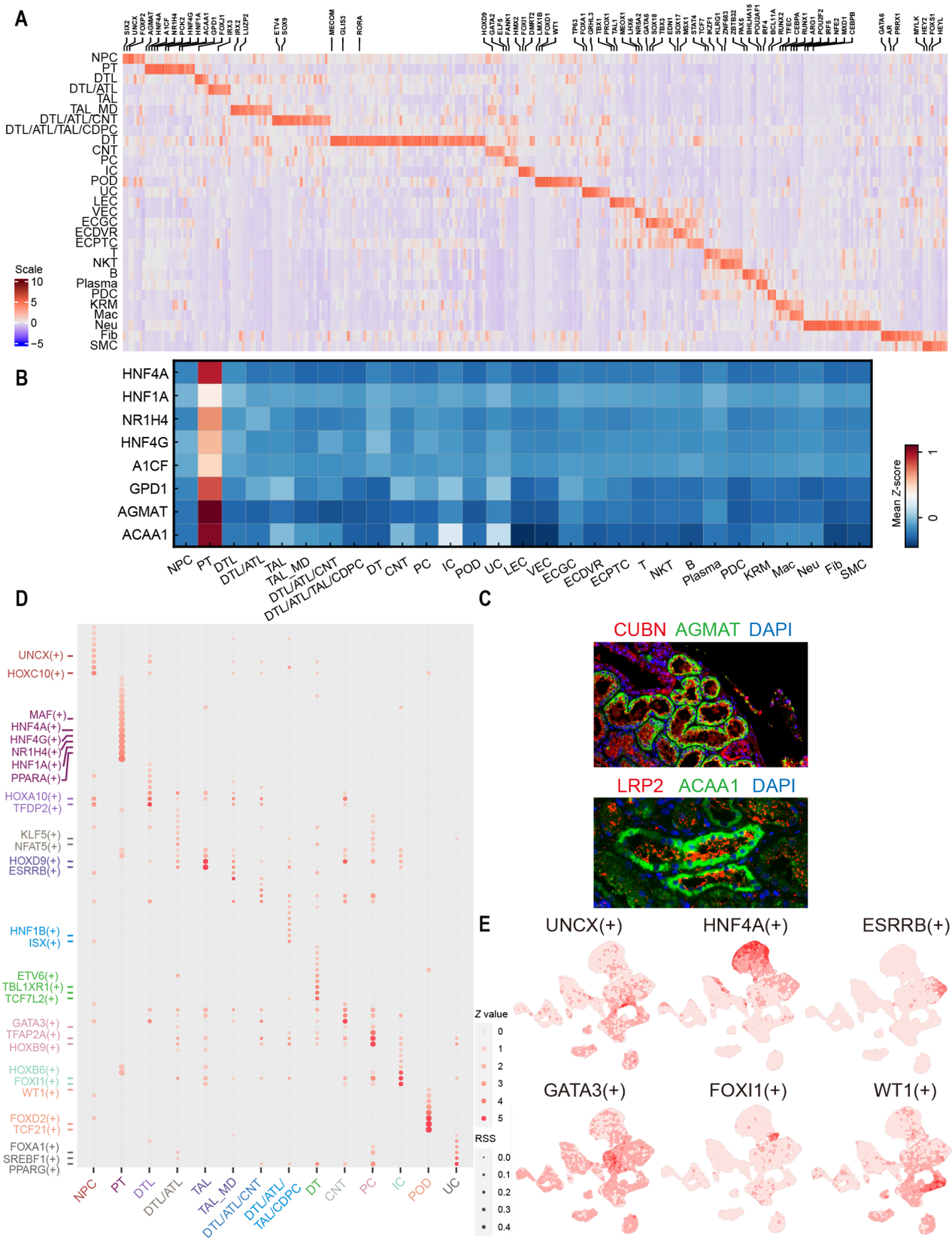

Figure 2 Cell type-specific TFs and regulatory landscape of the pig kidney

A: Heatmap showing expression of all cell-specific TFs. B: Heatmap showing TF expression of *HNF4A*, *HNF1A*, *NR1H4*, *HNF4G*, *A1CF*, *GPD1*, *AGMAT*, and *ACAA1* in all identified cell types. C: Fluorescence homologous double-label staining of paraffin sections of the renal cortex (RC) from Large White pigs during the pregnancy period with: Up: AGMAT (green), CUBN (red), and DAPI (blue) antibodies. Scale bars: 20 μm. Down: ACAA1 (green), LRP2 (red), and DAPI (blue) antibodies. Scale bars: 10 μm. D: Dot plot showing RSS and Z values of renal epithelial cell type-specific regulons. E: UMAP depiction of selected regulon activity.

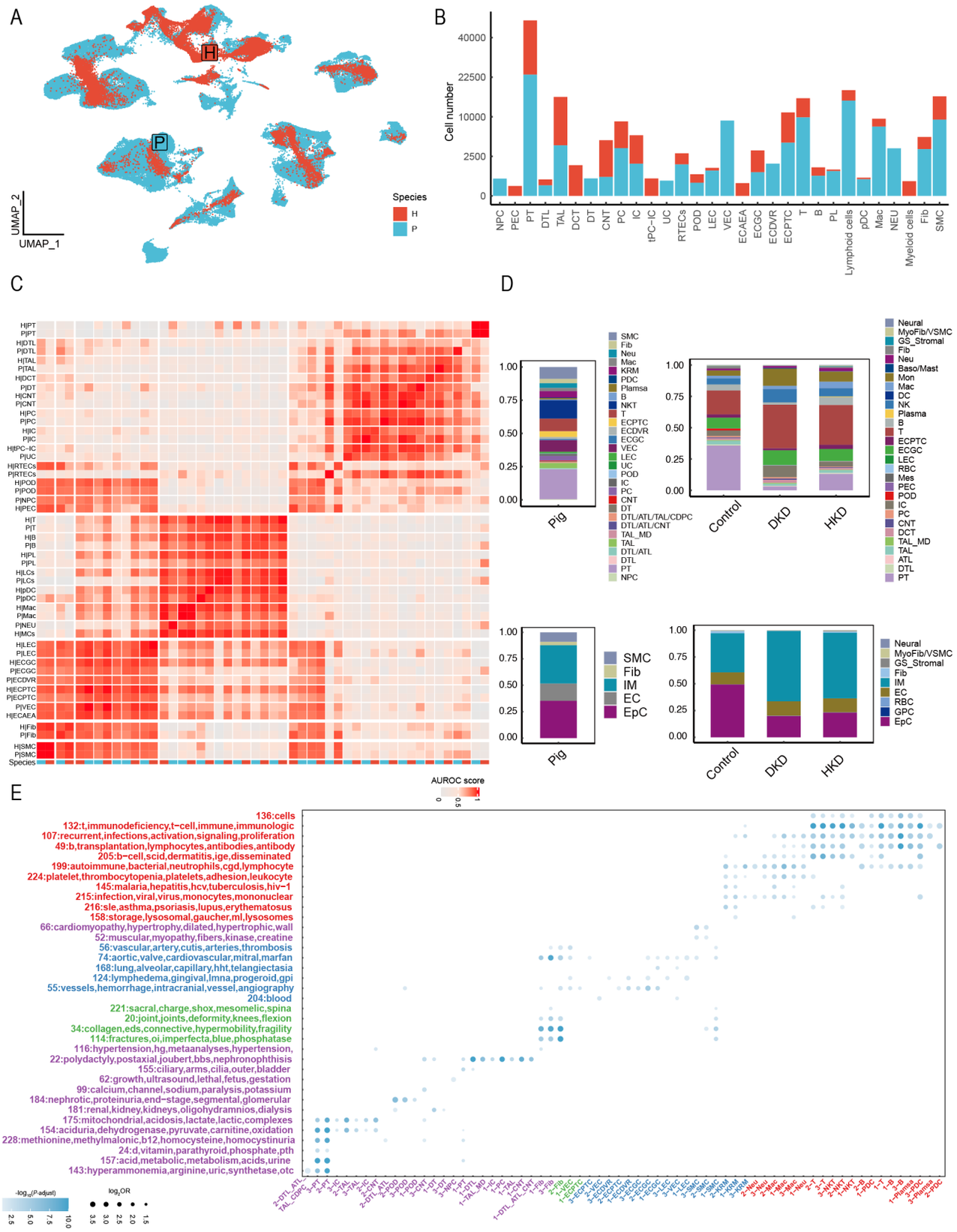

Figure 3 Human-pig cross-species comparison of kidney cell types

A: UMAP visualization of 124 952 cells, including 20 490 human and 104 462 pig kidney cells, colored by species. B: Bar plot showing species contribution to each annotated cell type. C: Heatmap showing AUROC scores between humans and pigs. AUROC scores were calculated using MetaNeighbor to assess cross-species cell type similarity. D: Bar plot showing cell type composition in pig kidneys, normal human kidneys, and diseased human kidneys. E: Dot plot showing the $-\log_{10}$ (*P*-adjust) and $\log_2$ (OR) values for each cell type across 36 representative OMIM disease topics. Horizontal axis denotes period-cell type associations (1 refers to E period; 2 refers to F period; 3 refers to P period), while the vertical axis denotes disease topics.

2022). To dissect the functional heterogeneity of TAL cells, 7 174 TAL cells were subjected to reclustering using the Harmony algorithm, identifying seven distinct TAL subtypes (Figure 4A; Supplementary Figure S5A, B). These subtypes featured high expression levels of TAL marker genes, such as *SLC12A1* and *UMOD*, confirming their identity (Figure 4D). To further characterize the functional properties of these TAL subtypes, pseudo-cell populations were generated by aggregating 50 TAL cells per subtype, followed by WGCNA (Langfelder & Horvath, 2008). Functional predictions were made based on pathway enrichment analysis of gene modules within each TAL cluster (Figure 4C; Supplementary Figure S5C). Several TAL subtypes exhibited multiperiod contributions, including TAL5, TAL3, and TAL0 (Figure 4B). TAL5 and TAL3, present across all three periods, were enriched in the yellow module, which was associated with monovalent inorganic cation homeostasis (Figure 4C). TAL0, primarily originating from the F and P periods, exhibited enrichment in the green module, which was associated with cellular amino acid metabolism, fatty acid response, and glycerolipid catabolism (Figure 4C). Notably, TAL0 showed high expression of *PON1*, a regulator of fatty acid metabolism, and *APOC3*, which plays a role in triglyceride homeostasis (Figure 4D). Distinct period-dependent heterogeneity was observed among TAL subtypes. TAL1, TAL4, and TAL6, primarily derived from the E period (Figure 4B), were enriched in the blue and pink modules, both involved in branching epithelium morphogenesis, kidney epithelium development, and nephron formation (Figure 4C). TAL1 and TAL6 exhibited high expression of S-shaped body nephron markers, including *PAPPA2*, *IRX1*, and *IRX2* (Lindström et al., 2021) (Figure 4D). Notably, TAL6, corresponding to the macula densa subtype, displayed high expression of genes regulating blood pressure, including *PTG2*, *NOS1*, and *AGTR1* (Figure 4D) (Harris et al., 1998; Zhang et al., 2015, 2021). This cluster was enriched in the red module, associated with nitric oxide metabolism and vasoconstriction regulation (Figure 4C). The TAL2 subtype, primarily derived from the P period, was enriched in the turquoise module, mainly associated with inflammatory response, innate immune response, and Toll-like receptor 4 signaling (Figure 4C). TAL2 exhibited high expression of antigen presentation genes, including *SLA-DRA*, *SLA-DRB1*, and *SLA-DQB1*, indicating a role in immune activation (Figure 4D). In addition, TAL2 exhibited high expression of *TLR2* and *TLR4*, which mediate innate immune defense against pathogens (Vallés et al., 2014), as well as *C1QA*, *C1QB*, and *C1QC*, which are involved in complement activation and inflammation (Janeway, 2001) (Figure 4D). This implies that TAL2 may function as an immune accessory cell type during pregnancy, contributing to pathogen defense and immune regulation. Notably, TAL2 exhibited greater similarity to human TAL cells in disease states, including CKD and AKI, compared to healthy conditions (Supplementary Figure S5D). This suggests that dysregulated immune activation in TAL2 during pregnancy may contribute to persistent renal injury.

Cell-cell interactions at the RC, RM, and RP sites

To investigate cell type enrichment across renal anatomical regions during pregnancy, the Speckle R package (Phipson et al., 2022) was used to assess significant spatial distributions. Results showed that PT cells were significantly enriched in the RC, whereas DTL/ATL and TAL cells were enriched in the RM and LEC, Fib, and SMC were highly represented in the RP (Figure 5A, B; Supplementary Table S6). Intercellular communication in the RC was analyzed using CellChat, revealing that IC, VEC, ECGC, and ECPTC exhibited a higher frequency of interactions (Figure 5C). Notably, IC engaged in signaling with EC, including ECGC, ECPTC, and VEC, via the *ADM-CALCRL* ligand-receptor (Figure 5D). Adrenomedullin (ADM) has been implicated in tubular diuresis and natriuresis, suggesting a functional role in fluid and electrolyte regulation (Nishikimi, 2007). KRM cells displayed distinct functional properties in different anatomical sites. In the RM, KRM cells primarily acted as signal receivers, whereas in the RP, they served as dominant signal senders (Figure 5E, G), indicating site-specific functional heterogeneity. Pathway enrichment analysis using the top 300 differentially expressed genes between RM-KRM and RP-KRM revealed distinct biological roles. In the RM, KRM were enriched in phagocytosis, myeloid leukocyte-mediated immunity, leukocyte activation, and antigen presentation via major histocompatibility (MHC) class II molecules, consistent with their role in immune surveillance (Figure 5I). Prior research suggests that medullary KRM encapsulate renal tubules to eliminate intratubular debris, ensuring unobstructed tubular flow (He et al., 2024). Cellular crosstalk analysis identified an interaction between TAL and KRM cells mediated by the *GAS6-MERTK* and *GAS6-AXL* ligand-receptor pairs (Figure 5F). *MERTK* and *AXL* are essential for apoptotic cell clearance, and *GAS6* enhances efferocytosis (Wanke et al., 2021). Stereo-seq analysis validated the colocalized expression of *GAS6*, *MERTK*, and *AXL* in the closely adjacent TAL and KRM cells, further supporting this functional interaction (Figure 5J; Supplementary Figure S6A–G). In contrast, KRM in the RP were functionally enriched in neutrophil migration, responses to bacterial molecules, and leukocyte migration pathways (Figure 5I). These macrophages mediated the innate immune response by secreting chemokines such as *CCL5*, *CCL8*, and *CCL14*, which bind to *CCR1* to recruit neutrophils (Figure 5H). Neutrophils, in turn, exhibit phagocytic and bactericidal activity, facilitating pathogen clearance in RP infections (Armbruster et al., 2018; Lacerda Mariano & Ingersoll, 2018).

DISCUSSION

The kidney plays a critical role in filtering blood, regulating electrolytes, and maintaining systemic homeostasis. It comprises a complex array of diverse cell types, each contributing to its physiological functions. In this study, a comprehensive single-cell transcriptomic atlas of the pig kidney was constructed, incorporating data from three anatomical sites and three periods. Our findings provide valuable insights into renal physiology and offer a comparative framework for human kidney research.

The PT is the primary site of glomerular filtrate processing, facilitating the reabsorption of nutrients, electrolytes, and water, while also performing glutamine hydrolysis to maintain acid-base balance and fatty acid oxidation for energy (Curthoys & Moe, 2014). PT cells exhibited high expression of metabolism-associated TFs including *GPD1*, *ACAA1*, and *AGMAT*, which was validated across multiple individuals, periods, and species. Given the substantial energy demands required to maintain osmotic gradients and active transport functions, PT cells rely on both glucose and fatty acid metabolism for sustained ATP production. *GPD1*, a cytoplasmic enzyme, catalyzes the conversion of

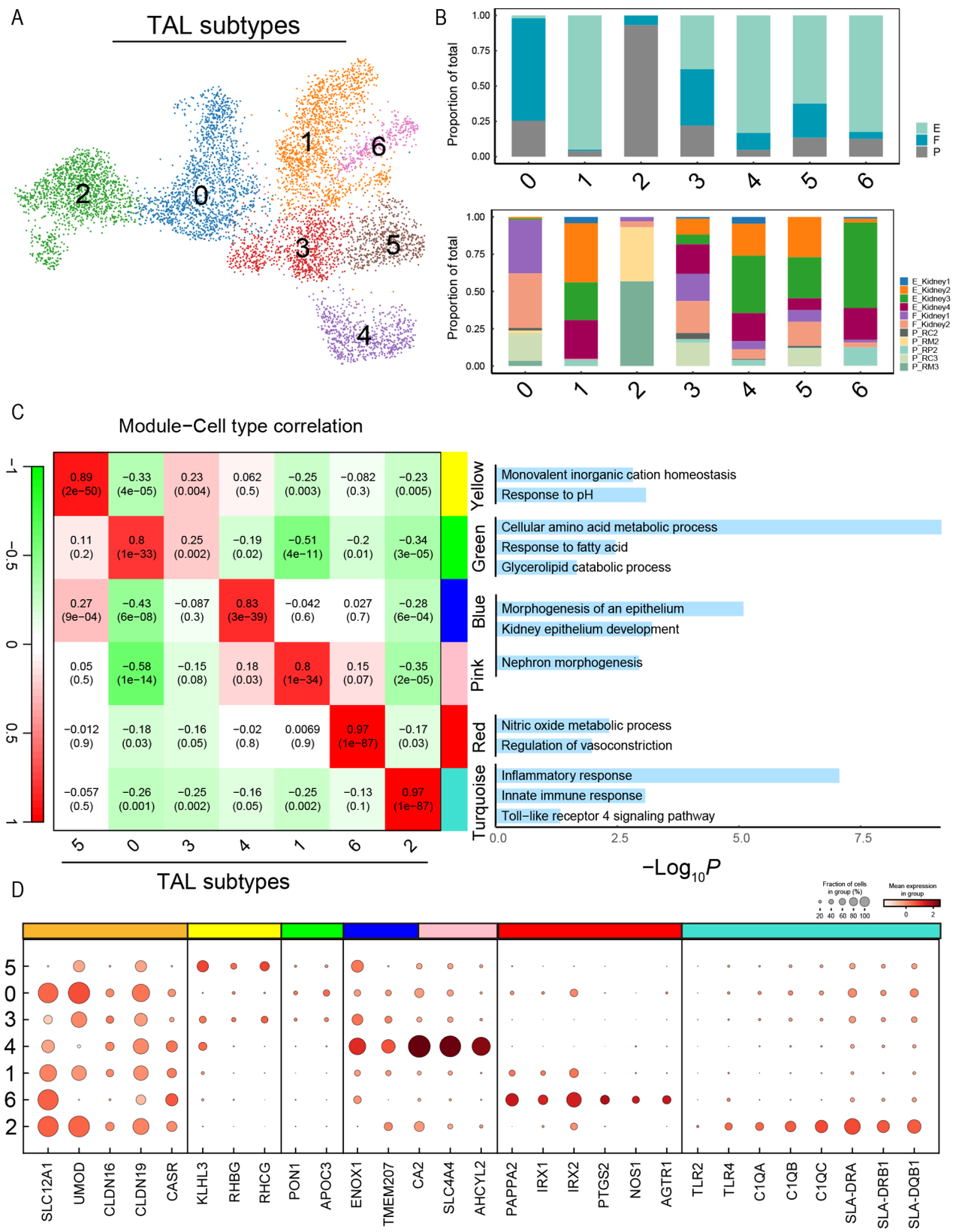

Figure 4 Heterogeneity of TAL cells

A: UMAP visualization of TAL cells, colored according to seven TAL subtypes. B: Up: Bar plot showing the contribution of each period to TAL subtypes. Down: Bar plot showing the distribution of TAL subtypes across anatomical sites. C: Left: Heatmap showing the correlation and significance of WGCNA modules associated with TAL subtypes. Right: Bar plot showing the pathways enriched in each identified WGCNA module. D: Dot plot showing representative gene expression profiles for each TAL subtype.

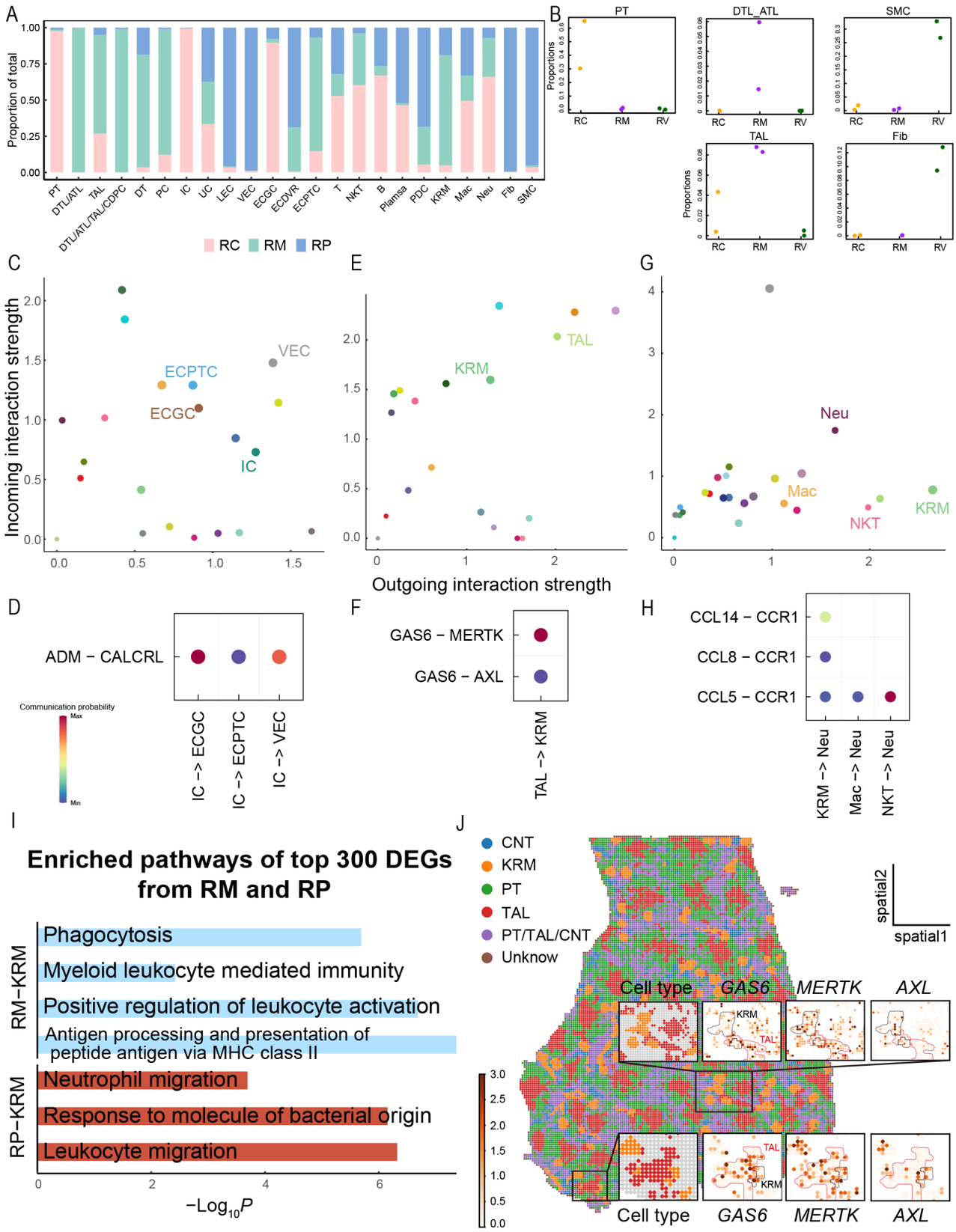

Figure 5 Cell-cell interactions across RC, RM, and RP anatomical sites

A: Bar plot showing the distribution of anatomical site compositions for each cell type. B: Scatter plot showing proportional distribution of cell types across the RC, RM, and RP. C, E, G: Scatter plot visualizing cell-cell interactions: Left (C), within the RC; Middle (E), within the RM; Right (G), within the RP. D, F, H: Dot plot showing significant ligand-receptor interactions: Left (D), IC with ECGC, ECPTC, and VEC; Middle (F), TAL with KRM; Right (H), KRM, Mac, and NKT with Neu. I: Bar plot showing enriched pathways in KRM cells at RM and RP, based on the top 300 differentially expressed genes (DEGs). J: Spatial distribution of annotated kidney cell types and expression of *GAS6*, *MERTK*, and *AXL* in TAL and KRM cells within selected regions.

dihydroxyacetone phosphate (DHAP) to glycerol-3-phosphate (G-3-P) while oxidizing *NADH* to NAD^+ (Zhou et al., 2023). The produced G-3-P is transported to the mitochondria to participate in oxidative phosphorylation and ATP synthesis via the electron transport chain. Acetyl coenzyme A acyltransferase-1 (*ACAA1*), a peroxisomal acyltransferase, plays a key role in fatty acid metabolism (Xiao et al., 2024a), further contributing to ATP production. The coordinated expression of *GPD1* and *ACAA1* in PT cells, particularly during the F and P periods, underscores the interdependence of glucose and fatty acid metabolism in energy homeostasis. These results suggest that *GPD1* and *ACAA1* may serve as fundamental and evolutionarily conserved regulators of metabolic function in PT cells, providing a reference for studies on PT cell metabolism and its implications for kidney function in both health and disease.

TAL cells assume a pivotal anatomical and functional role in renal physiology and electrolyte regulation (Balzer et al., 2022). To explore their functional heterogeneity, single-cell transcriptomic analysis identified seven TAL subtypes, each exhibiting distinct molecular signatures across multiple periods. During the E period, TAL1 and TAL4 were primarily associated with branching epithelium morphogenesis and epithelium development. TAL1 and TAL6 exhibited high expression of loop of Henle S-shaped body nephron markers, including *SLC12A1* and *PAPPA2*. Notably, *IRX1* and *IRX2*, transcriptional regulators predominantly expressed in the loop of Henle and macula densa (Lindström et al., 2021), were also detected in these clusters. The co-expression of *PAPPA2* with *IRX1* and *IRX2* suggests that TAL1 represents a progenitor-like population with the potential to differentiate into multiple distal nephron cell types, consistent with previous findings (Lindström et al., 2021). A distinct TAL2 subtype, primarily identified in adult pregnant sows, was validated across two independent RM samples and exhibited high expression of MHC class II molecules, including *SLA-DRA*, *SLA-DRB1*, and *SLA-DQB1*. These molecules are essential for antigen processing and presentation, facilitating T cell activation through inducible surface expression of MHC class II antigens, adhesion molecules, and costimulatory cytokines (Rubin-Kelley & Jevnikar, 1991; Wuthrich et al., 1990). Beyond its role in adaptive immunity, TAL2 exhibited high expression of genes associated with innate immunity, including Toll-like receptors (*TLR2* and *TLR4*) and complement system components (*C1QA*, *C1QB*, and *C1QC*). *TLR4* has been implicated in renal ischemia-reperfusion injury by promoting inflammation and apoptosis (Kim et al., 2005; Wu et al., 2007). Conversely, Tamm-Horsfall protein (THP), encoded by *UMOD*, may stabilize the outer medulla during renal injury by reducing inflammation, potentially through its influence on *TLR4* (El-Achkar et al., 2008). C1q, a crucial component of the classical complement pathway, is directly involved in the clearance of apoptotic cells, damaged cellular structures, and microbial pathogens. The up-regulation of C1q in TAL2 during pregnancy suggests a potential immune accessory role in renal defense, particularly in pathogen elimination, while also contributing to immune-mediated renal injury.

Cell type distribution across renal anatomical regions revealed distinct enrichment patterns in the RC, RM, and RP. PT cells were significantly enriched in the RC, while DTL/ATL and TAL cells were enriched in the RM and LEC, Fib, and SMC cells were highly represented in the RP. To further investigate functional differences among these anatomical sites, cell-cell interactions were analyzed, focusing on the KRM cell type (*C1QA*, *C1QC*, *CD81*, and *MS4A7*) (Yao et al., 2022; Zimmerman et al., 2019). KRM is *in situ* self-renewed and characterized by their phagocytic activities, expression of pattern recognition receptors (PRRs) and immunological regulation capacity, thus, maintaining kidney homeostasis. The current researches mainly focus on the heterogeneity of KRM at various development stages or under various physiological conditions (Epelman et al., 2014; Hoeffel et al., 2015; Lau et al., 2018; Lever et al., 2019; Wen et al., 2021; Yang et al., 2019; Yao et al., 2022; Zimmerman et al., 2020), where there are few studies on different anatomical sites. In the RM, KRM exhibited enrichment in phagocytosis, myeloid leukocyte-mediated immunity, leukocyte activation, and antigen presentation via MHC class II molecules. These findings align with previous observations indicating that KRM encapsulate renal tubules in the medullary region, facilitating the elimination of intratubular debris to maintain an unobstructed tubular system (He et al., 2024). Cellular crosstalk analysis identified a ligand-receptor interaction between TAL cells and KRM, mediated by *GAS6-MERTK* and *GAS6-AXL* signaling. *MERTK* and *AXL* are essential for apoptotic cell clearance, while *GAS6* enhances efferocytosis, thereby promoting tissue homeostasis (Wanke et al., 2021). The expression of *GAS6*, *MERTK*, and *AXL* in adjacent TAL and KRM cells was further validated utilizing Stereo-seq data, reinforcing their functional interplay. While KRM in RP enriched in neutrophil migration, response to molecule of bacterial origin, leukocyte migration. KRM could mediate innate immune response by secreting the chemokines like *CCL5*, *CCL8*, and *CCL14* bind the receptor *CCR1* to recruit the neutrophils which has the ability of phagocytosis and bactericidal activity to the site of the infection of the RP (Armbruster et al., 2018; Lacerda Mariano & Ingersoll, 2018).

DATA AVAILABILITY

The raw sequencing data were deposited in the China National Center for Bioinformation database of the Genome Sequence Archive (GSA) (CRA019075), NCBI database (BioProjectID PRJNA1218407), and Science Data Bank database (10.57760/sciencedb.20421)

SUPPLEMENTARY DATA

Supplementary data to this article can be found online.

COMPETING INTERESTS

The authors declare that they have no competing interests.

AUTHORS' CONTRIBUTIONS

L.S.H. conceptualized and designed the study. T.X.Y. was responsible for data quality control and analysis. T.X.Y. wrote the original draft. T.X.Y., N.L., and L.S.H. reviewed and revised the manuscript. T.X.Y. and N.L. were involved in experimental validation. L.S.H. supervised the project. All authors read and approved the final version of the manuscript.

ACKNOWLEDGMENTS

We thank our lab members (Bin Yang, Lin Rao, Yan-Yuan Xiao, Lei Xie, Si-Yu Yang, Xiao-Xiao Zou, Fei Huang, Li-Ping Cai, and Qing Zhang) for helpful discussions and Ying Su for preparing the antibodies for fluorescence homologous double-label staining of paraffin sections. In addition, we thank Hui-Qiong Zeng for drawing the pictures.

REFERENCES

Abedini A, Levinsohn J, Klötzer KA, et al. 2024. Single-cell multi-omic and spatial profiling of human kidneys implicates the fibrotic microenvironment

in kidney disease progression. *Nature Genetics*, **56**(8): 1712–1724.

Aibar S, González-Blas CB, Moerman T, et al. 2017. SCENIC: single-cell regulatory network inference and clustering. *Nature Methods*, **14**(11): 1083–1086.

Alpern RJ, Caplan MJ, Moe OW. 2012. Seldin and Giebisch's The Kidney: Physiology and Pathophysiology. 5th ed. Amsterdam: Elsevier.

Amberger JS, Bocchini CA, Scott AF, et al. 2019. OMIM. org: leveraging knowledge across phenotype-gene relationships. *Nucleic Acids Research*, **47**(D1): D1038–D1043.

Armbruster CE, Smith SN, Mody L, et al. 2018. Urine cytokine and chemokine levels predict urinary tract infection severity independent of uropathogen, urine bacterial burden, host genetics, and host age. *Infection and Immunity*, **86**(9): e00327–18.

Balzer MS, Rohacs T, Susztak K. 2022. How many cell types are in the kidney and what do they do?. *Annual Review of Physiology*, **84**: 507–531.

Beers K, Patel N. 2020. Kidney physiology in pregnancy. *Advances in Chronic Kidney Disease*, **27**(6): 449–454.

Bindea G, Mlecnik B, Hackl H, et al. 2009. ClueGO: a Cytoscape plug-in to decipher functionally grouped gene ontology and pathway annotation networks. *Bioinformatics*, **25**(8): 1091–1093.

Blomqvist SR, Vidarsson H, Fitzgerald S, et al. 2004. Distal renal tubular acidosis in mice that lack the forkhead transcription factor Foxi1. *The Journal of Clinical Investigation*, **113**(11): 1560–1570.

Cabili MN, Trapnell C, Goff L, et al. 2011. Integrative annotation of human large intergenic noncoding RNAs reveals global properties and specific subclasses. *Genes & Development*, **25**(18): 1915–1927.

Chen A, Liao S, Cheng MN, et al. 2022. Spatiotemporal transcriptomic atlas of mouse organogenesis using DNA nanoball-patterned arrays. *Cell*, **185**(10): 1777–1792. e21.

Cheung MD, Asiimwe R, Erman EN, et al. 2024. Spatiotemporal immune atlas of a clinical-grade gene-edited pig-to-human kidney xenotransplant. *Nature Communications*, **15**(1): 3140.

Cornelis T, Odutayo A, Keunen J, et al. 2011. The kidney in normal pregnancy and preeclampsia. *Seminars in Nephrology*, **31**(1): 4–14.

Cortal A, Martignetti L, Six E, et al. 2021. Gene signature extraction and cell identity recognition at the single-cell level with Cell-ID. *Nature Biotechnology*, **39**(9): 1095–1102.

Crow M, Paul A, Ballouz S, et al. 2018. Characterizing the replicability of cell types defined by single cell RNA-sequencing data using MetaNeighbor. *Nature Communications*, **9**(1): 884.

Curthoys NP, Moe OW. 2014. Proximal tubule function and response to acidosis. *Clinical Journal of the American Society of Nephrology*, **9**(9): 1627–1638.

Dura B, Choi JY, Zhang KR, et al. 2019. scFTD-seq: freeze-thaw lysis based, portable approach toward highly distributed single-cell 3′ mRNA profiling. *Nucleic Acids Research*, **47**(3): e16.

El-Achkar TM, Eadon MT, Menon R, et al. 2021. A multimodal and integrated approach to interrogate human kidney biopsies with rigor and reproducibility: guidelines from the Kidney Precision Medicine Project. *Physiological Genomics*, **53**(1): 1–11.

El-Achkar TM, Wu XR, Rauchman M, et al. 2008. Tamm-horsfall protein protects the kidney from ischemic injury by decreasing inflammation and altering TLR4 expression. *American Journal of Physiology-Renal Physiology*, **295**(2): F534–F544.

Epelman S, Lavine KJ, Randolph GJ. 2014. Origin and functions of tissue macrophages. *Immunity*, **41**(1): 21–35.

Eraslan G, Drokhlyansky E, Anand S, et al. 2022. Single-nucleus cross-tissue molecular reference maps toward understanding disease gene function. *Science*, **376**(6594): eabl4290.

Festuccia N, Owens N, Navarro P. 2018. Esrrb, an estrogen-related receptor involved in early development, pluripotency, and reprogramming. *FEBS Letters*, **592**(6): 852–877.

Fischer MJ. 2007. Chronic kidney disease and pregnancy: maternal and fetal outcomes. *Advances in Chronic Kidney Disease*, **14**(2): 132–145.

Franzén O, Gan LM, Björkegren JLM. 2019. PanglaoDB: a web server for exploration of mouse and human single-cell RNA sequencing data. *Database*, **2019**: baz046.

Geirsdottir L, David E, Keren-Shaul H, et al. 2019. Cross-species single-cell analysis reveals divergence of the primate microglia program. *Cell*, **179**(7): 1609–1622. e16.

Grassmeyer J, Mukherjee M, Deriso J, et al. 2017. Elf5 is a principal cell lineage specific transcription factor in the kidney that contributes to *Aqp2* and *Avpr2* gene expression. *Developmental Biology*, **424**(1): 77–89.

Guyton AC, Hall JE. 2005. Textbook of Medical Physiology. 11th ed. Philadelphia: Elsevier Saunders.

Han L, Wei XY, Liu CY, et al. 2022. Cell transcriptomic atlas of the non-human primate *Macaca fascicularis*. *Nature*, **604**(7907): 723–731.

Hao J, Cao W, Huang J, et al. 2019. Optimal Gene Filtering for Single-Cell data (OGFSC)-a gene filtering algorithm for single-cell RNA-seq data. *Bioinformatics*, **35**(15): 2602–2609.

Hao YH, Hao S, Andersen-Nissen E, et al. 2021. Integrated analysis of multimodal single-cell data. *Cell*, **184**(13): 3573–3587. e29.

Harris RC, Wang JL, Cheng HF, et al. 1998. Prostaglandins in macula densa function. *Kidney International*, **54**(67): S49–S52.

He J, Cao YY, Zhu Q, et al. 2024. Renal macrophages monitor and remove particles from urine to prevent tubule obstruction. *Immunity*, **57**(1): 106–123. E7.

Hoeffel G, Chen JM, Lavin Y, et al. 2015. C-Myb^{+} erythro-myeloid progenitor-derived fetal monocytes give rise to adult tissue-resident macrophages. *Immunity*, **42**(4): 665–678.

Huang LY, Wang HL, Zhou YR, et al. 2016. Apobec-1 complementation factor (A1CF) inhibits epithelial-mesenchymal transition and migration of normal rat kidney proximal tubular epithelial cells. *International Journal of Molecular Sciences*, **17**(2): 197.

Janeway C. 2001. Immunobiology: the Immune System in Health and Disease. 5th ed. New York: Garland Pub.

Jim B, Garovic VD. 2017. Acute kidney injury in pregnancy. *Seminars in Nephrology*, **37**(4): 378–385.

Jin SQ, Guerrero-Juarez CF, Zhang LH, et al. 2021. Inference and analysis of cell-cell communication using CellChat. *Nature Communications*, **12**(1): 1088.

Kim BS, Lim SW, Li C, et al. 2005. Ischemia-reperfusion injury activates innate immunity in rat kidneys. *Transplantation*, **79**(10): 1370–1377.

Korsunsky I, Millard N, Fan J, et al. 2019. Fast, sensitive and accurate integration of single-cell data with Harmony. *Nature Methods*, **16**(12): 1289–1296.

Lacerda Mariano L, Ingersoll MA. 2018. Bladder resident macrophages: mucosal sentinels. *Cellular Immunology*, **330**: 136–141.

Lake BB, Menon R, Winfree S, et al. 2023. An atlas of healthy and injured cell states and niches in the human kidney. *Nature*, **619**(7970): 585–594.

Langfelder P, Horvath S. 2008. WGCNA: an R package for weighted correlation network analysis. *BMC Bioinformatics*, **9**: 559.

Latchman DS. 1997. Transcription factors: an overview. *The International Journal of Biochemistry & Cell Biology*, **29**(12): 1305–1312.

Lau A, Chung H, Komada T, et al. 2018. Renal immune surveillance and dipeptidase-1 contribute to contrast-induced acute kidney injury. *The Journal of Clinical Investigation*, **128**(7): 2894–2913.

Lever JM, Hull TD, Boddu R, et al. 2019. Resident macrophages reprogram toward a developmental state after acute kidney injury. *JCI Insight*, **4**(2): e125503.

Levine JH, Simonds EF, Bendall SC, et al. 2015. Data-driven phenotypic dissection of aml reveals progenitor-like cells that correlate with prognosis. *Cell*, **162**(1): 184–197.

Lindström NO, Sealfon R, Chen X, et al. 2021. Spatial transcriptional mapping of the human nephrogenic program. *Developmental Cell*, **56**(16): 2381–2398. e6.

Liu SY, Zhao Y, Lu S, et al. 2023. Single-cell transcriptomics reveals a mechanosensitive injury signaling pathway in early diabetic nephropathy. *Genome Medicine*, **15**(1): 2.

Lunney JK, Van Goor A, Walker KE, et al. 2021. Importance of the pig as a

human biomedical model. *Science Translational Medicine*, **13**(621): eabd5758.
Marable SS, Chung E, Park JS. 2020. *Hnf4a* is required for the development of Cdh6-expressing progenitors into proximal tubules in the mouse kidney. *Journal of the American Society of Nephrology*, **31**(11): 2543–2558.
Miao J, Zhu HH, Wang JN, et al. 2024. Experimental models for preclinical research in kidney disease. *Zoological Research*, **45**(5): 1161–1174.
Miao Z, Balzer MS, Ma ZY, et al. 2021. Single cell regulatory landscape of the mouse kidney highlights cellular differentiation programs and disease targets. *Nature Communications*, **12**(1): 2277.
Muto Y, Wilson PC, Ledru N, et al. 2021. Single cell transcriptional and chromatin accessibility profiling redefine cellular heterogeneity in the adult human kidney. *Nature Communications*, **12**(1): 2190.
Nishikimi T. 2007. Adrenomedullin in the kidney-renal physiological and pathophysiological roles. *Current Medicinal Chemistry*, **14**(15): 1689–1699.
Park J, Shrestha R, Qiu CX, et al. 2018. Single-cell transcriptomics of the mouse kidney reveals potential cellular targets of kidney disease. *Science*, **360**(6390): 758–763.
Phipson B, Sim CB, Porrello ER, et al. 2022. *propeller*: testing for differences in cell type proportions in single cell data. *Bioinformatics*, **38**(20): 4720–4726.
Qu J, Yang F, Zhu T, et al. 2022. A reference single-cell regulomic and transcriptomic map of cynomolgus monkeys. *Nature Communications*, **13**(1): 4069.
Rao L, Cai LP, Huang LS. 2023. Single-cell dynamics of liver development in postnatal pigs. *Science Bulletin*, **68**(21): 2583–2597.
Reynolds G, Vegh P, Fletcher J, et al. 2021. Developmental cell programs are co-opted in inflammatory skin disease. *Science*, **371**(6527): 394.
Rubin-Kelley VE, Jevnikar AM. 1991. Antigen presentation by renal tubular epithelial cells. *Journal of the American Society of Nephrology*, **2**(1): 13–26.
Stewart BJ, Ferdinand JR, Young MD, et al. 2019. Spatiotemporal immune zonation of the human kidney. *Science*, **365**(6460): 1461–1466.
Suo SB, Zhu Q, Saadatpour A, et al. 2018. Revealing the critical regulators of cell identity in the mouse cell atlas. *Cell Reports*, **25**(6): 1436–1445. e3.
Szczepanski J, Griffin A, Novotny S, et al. 2020. Acute kidney injury in pregnancies complicated with preeclampsia or HELLP syndrome. *Frontiers in Medicine*, **7**: 22.
Tabula Sapiens Consortium, Jones RC, Karkanias J, et al. 2022. The Tabula Sapiens: a multiple-organ, single-cell transcriptomic atlas of humans. *Science*, **376**(6594): eabl4896.
The Tabula Muris Consortium, Overall Coordination, Logistical Coordination, et al. 2018. Single-cell transcriptomics of 20 mouse organs creates a *Tabula Muris*. *Nature*, **562**(7727): 367–372.
Uchida S, Matsumura Y, Rai T, et al. 1997. Regulation of aquaporin-2 gene transcription by GATA-3. *Biochemical and Biophysical Research Communications*, **232**(1): 65–68.
Uhlén M, Fagerberg L, Hallström BM, et al. 2015. Proteomics. Tissue-based map of the human proteome. *Science*, **347**(6220): 1260419.
Vallés PG, Lorenzo AG, Bocanegra V, et al. 2014. Acute kidney injury: what part do toll-like receptors play?. *International Journal of Nephrology and Renovascular Disease*, **7**: 241–251.
Van de Sande B, Flerin C, Davie K, et al. 2020. A scalable SCENIC workflow for single-cell gene regulatory network analysis. *Nature Protocols*, **15**(7): 2247–2276.
van de Velde M, Scholefield H, Plante LA. 2013. Maternal Critical Care: a multidisciplinary Approach. Cambridge: Cambridge University Press.
Wanders RJ, Vreken P, Ferdinandusse S, et al. 2001. Peroxisomal fatty acid α- and *β*-oxidation in humans: enzymology, peroxisomal metabolite transporters and peroxisomal diseases. *Biochemical Society Transactions*, **29**(Pt 2): 250–267.
Wang F, Ding PW, Liang X, et al. 2022. Endothelial cell heterogeneity and microglia regulons revealed by a pig cell landscape at single-cell level. *Nature Communications*, **13**(1): 3620.
Wang JJ, Sun HY, Jiang MM, et al. 2021a. Tracing cell-type evolution by cross-species comparison of cell atlases. *Cell Reports*, **34**(9): 108803.
Wang YL, Li X, Cao Y, et al. 2021b. Effect of the *ACAA1* gene on preadipocyte differentiation in sheep. *Frontiers in Genetics*, **12**: 649140.
Wanke F, Gutbier S, Rümmelin A, et al. 2021. Ligand-dependent kinase activity of MERTK drives efferocytosis in human iPSC-derived macrophages. *Cell Death & Disease*, **12**(6): 538.
Wen Y, Yan HR, Wang B, et al. 2021. Macrophage heterogeneity in kidney injury and fibrosis. *Frontiers in Immunology*, **12**: 681748.
Wolf FA, Angerer P, Theis FJ. 2018. SCANPY: large-scale single-cell gene expression data analysis. *Genome Biology*, **19**(1): 15.
Wolock SL, Lopez R, Klein AM. 2019. Scrublet: computational identification of cell doublets in single-cell transcriptomic data. *Cell Systems*, **8**(4): 281–291. e29.
Wu HL, Chen G, Wyburn KR, et al. 2007. TLR4 activation mediates kidney ischemia/reperfusion injury. *The Journal of Clinical Investigation*, **117**(10): 2847–2859.
Wuthrich RP, Glimcher LH, Yui MA, et al. 1990. MHC class II, antigen presentation and tumor necrosis factor in renal tubular epithelial cells. *Kidney International*, **37**(2): 783–792.
Xiao MM, Ruan Y, Huang JJ, et al. 2024a. Association analysis between Acetyl-Coenzyme A Acyltransferase-1 gene polymorphism and growth traits in Xiangsu pigs. *Frontiers in Genetics*, **15**: 1346903.
Xiao YY, Zhang Q, Huang F, et al. 2024b. Single-cell profiling of the pig cecum at various developmental stages. *Zoological Research*, **45**(1): 55–68.
Yanai I, Benjamin H, Shmoish M, et al. 2005. Genome-wide midrange transcription profiles reveal expression level relationships in human tissue specification. *Bioinformatics*, **21**(5): 650–659.
Yang Q, Wang YX, Pei GC, et al. 2019. Bone marrow-derived Ly6C$^-$ macrophages promote ischemia-induced chronic kidney disease. *Cell Death & Disease*, **10**(4): 291.
Yang SY, Chen D, Xie L, et al. 2023. Developmental dynamics of the single nucleus regulatory landscape of pig hippocampus. *Science China Life Sciences*, **66**(11): 2614–2628.
Yao WJ, Chen Y, Li ZH, et al. 2022. Single cell RNA sequencing identifies a unique inflammatory macrophage subset as a druggable target for alleviating acute kidney injury. *Advanced Science*, **9**(12): e2103675.
Young RA. 2011. Control of the embryonic stem cell state. *Cell*, **144**(6): 940–954.
Zhang HT, Unal H, Gati C, et al. 2015. Structure of the angiotensin receptor revealed by serial femtosecond crystallography. *Cell*, **161**(4): 833–844.
Zhang J, Wang XM, Cui Y, et al. 2021. Knockout of macula densa neuronal nitric oxide synthase increases blood pressure in db/db Mice. *Hypertension*, **78**(6): 1760–1770.
Zhang LK, Ma HD, Guo M, et al. 2022. Dynamic transcriptional atlas of male germ cells during porcine puberty. *Zoological Research*, **43**(4): 600–603.
Zhou W, Simic P, Zhou IY, et al. 2023. Kidney glycolysis serves as a mammalian phosphate sensor that maintains phosphate homeostasis. *The Journal of Clinical Investigation*, **133**(8): e164610.
Zimmerman KA, Bentley MR, Lever JM, et al. 2019. Single-cell RNA sequencing identifies candidate renal resident macrophage gene expression signatures across species. *Journal of the American Society of Nephrology*, **30**(5): 767–781.
Zimmerman KA, Huang JF, He L, et al. 2020. Interferon regulatory factor-5 in resident macrophage promotes polycystic kidney disease. *Kidney360*, **1**(3): 179–190.